1997

Turbulence Modeling of the Toroidal Wall Heat Load Due to Shear Flows over Cavities in the Neutral Gas Blanket Divertor Regime

George Vahala

Linda L. Vahala
Old Dominion University, lvahala@odu.edu

Joseph Morrison

Turbulence modeling of the toroidal wall heat load due to shear flows over cavities in the neutral gas blanket divertor regime

George Vahala
Department of Physics, William & Mary, Williamsburg, Virginia 23187 Institute for Computer Applications in Science and Engineering, NASA-Langley, Hampton, Virginia 23666

Linda Vahala
Department of Electrical and Computer Engineering, Old Dominion University, Norfolk, Virginia 23529

Joseph Morrison
Analytical Services and Materials, Incorporated, Hampton, Virginia 23666

Heat loads to the target plate in reactor tokamaks are estimated to be orders of magnitude higher than those that can be withstood by known materials. In regimes of plasma detachment, there is strong evidence that plasma recombination occurs near the divertor plate, leading to a cold neutral gas blanket. Because of the strong coupling between the plasma and the neutrals within the divertor region, there is significant neutral flows along field lines up to Mach 1.2 and Reynolds numbers over 1000. Here the effects of three dimensional (3D) neutral turbulence within the gas blanket on heat deposition to the toroidal wall are examined. Both two dimensional (2D) mean shear flows over toroidal cavities as well as a fully 3D initial value problem of heat pulse propagation are considered. The results for algebraic stress model, K-ϵ and laminar flows are compared. It is found that 3D velocity shear turbulence has profound effects on the heat loads, indicating that simple (linear) Reynolds stress closure schemes are inadequate. © *1997 American Institute of Physics.* [S1070-664X(97)01311-6]

I. INTRODUCTION

Projected heat loads onto the divertor plate in reactor tokamaks are a major cause of concern.[1] While the idea of a gas blanket itself is quite old[2] and the possible role of plasma turbulence and plasma neutralization in wall plasma physics has been recently reviewed,[3] plasma recombination[4] has now been shown to play an important role in the formation of a cold neutral gas blanket between the divertor plate and the plasma flame front in the scrape-off layer (SOL). Previously, not much attention had been given to plasma recombination processes since they can only play a major role in regimes where the temperatures are on the order of 1 eV. To explain the recent experimental results on the so-called detached divertor regime[5] (in which the plasma essentially extinguishes itself near the divertor plate), recent plasma divertor models[6] required plasma temperatures around 1 eV near the divertor plate. Moreover, such low plasma-divertor temperatures have been verified experimentally[7] and the role of plasma recombination in observed plasma detachment has been recently reviewed.[8]

With plasma recombination and neutral gas ionization within the divertor region, there is strong coupling between the plasma dynamics and neutral fluid flow.[6] Since the plasma flows principally along the magnetic field, the neutral flow will also be along the field lines—and in recent two dimensional (2D) laminar simulations[6] for coupled plasma-neutral flows, this neutral gas velocity can readily exceed Mach 1, with Reynolds numbers of the order of 1000. Now recent fluid experiments[9] have succeeded in triggering turbulence in channel flow at Reynolds numbers as low as 650 by using eddy promoters. Turbulence in the cold gas blanket will lead to enhanced heat removal and more efficient redis-tribution of the heat flux onto the toroidal side walls and away from the divertor plate. It is the purpose of this article to not only extend our previous calculations[10] to more sophisticated turbulence closure models but to initiate an investigation of the effect of 3D mean shear flows on the wall heat loads.

There are three basic simulation techniques[11] to fluid turbulence: direct numerical simulations (DNS), large eddy simulations (LES), and Reynolds-averaged navier stokes (RANS). Each method has its strengths and limitations because turbulence is three dimensional (3D) and intrinsically involves disturbances on all length scales. DNS resolves all turbulent scales: from the large scale eddies down to the dissipation range eddies without any approximations. As a result, DNS is limited to low Reynolds number turbulence and simple geometry due to the limitations of computer memory and speed. While the Reynolds number for our divertor problem is quite low, the geometry is quite complex and cannot be readily handled by DNS on present or foreseeable computer architectures. In LES, a suitable grid is chosen that allows one to resolve the large eddies but forces one to model the smaller scale structures and their interactions with the large scale eddies. One of the advantages gained in LES is that the small scale turbulence tends to be isotropic and thus lend themselves to easier modeling. While this increases the range of geometric flows that can be handled and somewhat increases the range of Reynolds number, LES is found to be only factors of 5–8 faster than DNS. The other problem facing both DNS and LES is the need to obtain a sufficiently large sampling of the flow statistics—especially for inhomogeneous flows.

Here, we apply RANS to compressible turbulence. In

RANS, all the turbulent scales are time averaged over an interval short compared to mean flow time variations. All the turbulence effects on the mean flow are modeled—leading to somewhat complex turbulence models since one is now modeling even the large turbulent scales. The averaged momentum equation is not closed because of the presence of the Reynolds stress tensor τ_{ij}. The simplest two-equation models determine equations for the turbulent kinetic energy $K = 1/2\,\mathrm{Tr}\,\tau$ and the turbulent dissipation rate ϵ. If a simple gradient transport hypothesis is imposed on the off-diagonal Reynolds stress tensor τ_{ij}, the Boussinesq (linear in the mean flow gradients) approximation is obtained. We shall call the resulting RANS model the K-ϵ model, and it was this K-ϵ model that we[10] considered in our earlier 2D mean flow calculations of heat deposition for various toroidal cavity geometries. However, more sophisticated closure schemes for the Reynolds stress tensor have been developed. We shall consider one of these schemes called algebraic stress model (ASM). In the ASM, the τ_{ij} elements are modeled with higher order (nonlinear in the mean flow gradients) corrections to the Boussinesq approximation.

In Sec. II, we briefly state the K-ϵ and ASM equations and refer the reader to the literature[12] for more details. In Sec. III, we revisit the problem of 2D mean flow over toroidal cavities and compare the K-ϵ and ASM results for the steady state toroidal wall heat deposition. In Sec. IV, we set up the problem for 3D mean flow over toroidal cavities—where we now not only consider the toroidal flow but now include the poloidal flow towards the divertor plate as well. Heat depositions to the toroidal wall are again calculated for both the K-ϵ and ASM closures for the initial value problem of a heat pulse propagating towards the divertor plate. The time evolution of these heat deposition profiles are also contrasted to those determined from laminar 3D mean flows. We briefly discuss the numerical code in Sec. V and summarize our results in Sec. VI.

II. RANS CLOSURE MODELS

In RANS, one introduces time averages over turbulent fluctuations on some function $f(x,t)$ by

$$\langle f\rangle \equiv \frac{1}{T}\int_0^T dt\,f(x,t),\tag{1}$$

where T is a time interval long on the turbulent fluctuation time scales, but short on the mean-flow time scale. Thus f is decomposed into a Reynolds-average mean $\langle f\rangle$ and the Reynolds-averaged fluctuation f':

$$f(x,t)=\langle f\rangle + f'\tag{2}$$

Since we will be dealing with compressible flows, it is very convenient to introduce density-weighted Reynolds averages (called Favre averages)[13]

$$\ll f\gg \equiv \frac{\langle \rho f\rangle}{\langle \rho\rangle},\tag{3}$$

where ρ is the density. The Favre fluctuations are

$$f(x,t)=\ll f\gg + f''.\tag{4}$$

The RANS equations for the evolution of density, momentum and energy are[11]

$$\frac{\partial}{\partial t}\langle\rho\rangle + \frac{\partial}{\partial x_\alpha}(\langle\rho\rangle\ll u_\alpha\gg)=0\tag{5}$$

$$\frac{\partial}{\partial t}(\langle\rho\rangle\ll u_i\gg) + \frac{\partial}{\partial x_\alpha}(\langle\rho\rangle\ll u_i\gg \ll u_\alpha\gg + \langle p\rangle\delta_{i\alpha})$$
$$=\frac{\partial\langle\sigma_{i\alpha}\rangle}{\partial x_\alpha} - \frac{\partial\langle\rho\rangle\tau_{i\alpha}}{\partial x_\alpha}\tag{6}$$

$$\frac{\partial}{\partial t}(\langle\rho\rangle\ll E\gg) + \frac{\partial}{\partial x_\alpha}[\ll u_\alpha\gg(\langle\rho\rangle\ll E\gg + \langle p\rangle)]$$
$$=\frac{\partial}{\partial x_\alpha}\langle\sigma_{\alpha\beta}\rangle\ll u_\alpha\gg - \langle q_\alpha\rangle) + \frac{\partial}{\partial x_\alpha}(\langle\sigma_{\alpha\beta}\rangle\langle u''_\beta\rangle$$
$$+\langle\sigma'_{\alpha\beta}u'_\beta\rangle - \langle\rho\rangle\ll E''u''_\alpha\gg),\tag{7}$$

where the mean viscous stress tensor and heat flux are

$$\langle\sigma_{ij}\rangle = -\frac{2}{3}\left\langle\mu\frac{\partial u_\alpha}{\partial x_\alpha}\right\rangle\delta_{ij} + \left\langle\mu\left(\frac{\partial u_i}{\partial x_j}+\frac{\partial u_j}{\partial x_i}\right)\right\rangle\tag{8}$$

$$\langle q_i\rangle = -\left\langle\kappa\frac{\partial T}{\partial x_i}\right\rangle.\tag{9}$$

μ is the viscosity and κ the thermal conductivity. The Favre-averaged total energy

$$\ll E\gg = c_v\ll T\gg + \frac{1}{2}\ll u_\alpha\gg \ll u_\alpha\gg + \frac{1}{2}\ll u''_\alpha u''_\alpha\gg\tag{10}$$

is employed so that shock-capturing techniques can be efficiently coded into the numerical algorithm. Throughout this article, the summation convention is used for repeated subscripts—which are typically written with Greek characters. The equation of state is

$$\langle p\rangle = (\gamma-1)\langle\rho\rangle\left(\ll E\gg - \frac{1}{2}\ll u\gg^2 - K\right),\tag{11}$$

where γ is the ratio of specific heats.

While the density Eq. (5) is form invariant under RANS, there are closure questions due to the last terms in the RANS momentum and energy equations: the Favre-averaged Reynolds stress tensor

$$\tau_{ij}=\ll u''_i u''_j\gg\tag{12}$$

and the energy-velocity fluctuation correlation

$$\langle\rho\rangle\ll E''u''_i\gg = c_v\langle\rho\rangle\ll u''_i T''\gg + \langle\rho\rangle\ll u_\alpha\gg \tau_{i\alpha}$$
$$+\frac{1}{2}\langle\rho\rangle\ll u''_\alpha u''_\alpha u''_i\gg.\tag{13}$$

While an evolution equation can be derived for the Reynolds stress tensor, such second-order closure schemes require the modeling of many unknown turbulent quantities. Moreover, such schemes are not only computationally expensive but are prone to numerical instabilities due to the absence of a turbulent viscosity. A more robust closure scheme is the two-equation model in which one determines

the time evolution of the turbulent kinetic energy (which is nothing but the trace of the Reynolds stress tensor)

$$K = \frac{1}{2} \tau_{\alpha\alpha} \tag{14}$$

(with the usual summation over repeated Greek subscripts), and the turbulent dissipation rate

$$\epsilon = \left\langle \sigma'_{\alpha\beta} \frac{\partial u'_{\alpha}}{\partial x_{\beta}} \right\rangle. \tag{15}$$

These transport equations are

$$\frac{\partial(\langle\rho\rangle K)}{\partial t} + \frac{\partial(\langle\rho\rangle \ll u_{\alpha}\gg K)}{\partial x_{\alpha}}$$

$$= -\langle\rho\rangle \tau_{\alpha\beta} \frac{\partial \ll u_{\alpha}\gg}{\partial x_{\beta}} - \langle\rho\rangle\epsilon + \frac{\partial}{\partial x_{\alpha}}\left[\left(\mu + \frac{\langle\mu_{TL}\rangle}{\sigma_k}\right)\frac{\partial K}{\partial x_{\alpha}}\right] \tag{16}$$

and

$$\frac{\partial(\langle\rho\rangle \epsilon)}{\partial t} + \frac{\partial(\langle\rho\rangle \ll u_{\alpha}\gg \epsilon)}{\partial x_{\alpha}}$$

$$= -\langle\rho\rangle C_{\epsilon1} \frac{\epsilon}{K} \tau_{\alpha\beta} \frac{\partial \ll u_{\alpha}\gg}{\partial x_{\beta}} - \langle\rho\rangle C_{\epsilon2} f \frac{\epsilon^2}{K}$$

$$+ \frac{\partial}{\partial x_{\alpha}}\left[\left(\mu + \frac{\langle\mu_{TL}\rangle}{\sigma_{\epsilon}}\right)\frac{\partial \epsilon}{\partial x_{\alpha}}\right], \tag{17}$$

where μ is the molecular viscosity, and $\langle\mu_{TL.}\rangle$ is the eddy viscosity with corrections for the logarithmic layer near the wall

$$\langle\mu_{TL}\rangle = C_{\mu L}\langle\rho\rangle \frac{K^2}{\epsilon}, \quad \text{with} \quad C_{\mu L} = 0.081 \tag{18}$$

and the function f is introduced to remove the singularity at the wall. A critical issue is the modeling of the Reynolds stress tensor τ_{ij}. Since second-order closure models are deduced on stronger theoretical grounds than the lower level models, they can be used to derive better two-equation models as in the algebraic stress model (ASM).[14,15] We shall compare the ASM with the simpler gradient transport closure model which we shall call here the K-ϵ model.

A. Algebraic stress model (ASM)

Using the idea[16] of a tensorial polynomial expansion for obtaining explicit algebraic stress, one can obtain the following nonlinear representation[14]

$$\langle\rho\rangle \tau_{ij} = \frac{2}{3}\langle\rho\rangle K \delta_{ij} - 2\langle\mu_T\rangle\left[\left(S_{ij} - \frac{1}{3}S_{\alpha\alpha}\delta_{ij}\right)\right.$$

$$+ \frac{\alpha_4 K}{\epsilon}(S_{i\alpha}W_{\alpha j} + S_{j\alpha}W_{\alpha i})$$

$$\left. - \frac{\alpha_5 K}{\epsilon}\left(S_{i\alpha}S_{\alpha j} - \frac{1}{3}S_{\alpha\beta}S_{\alpha\beta}\delta_{ij}\right)\right] \tag{19}$$

but here we use the near wall eddy viscosity coefficient[15]

$$\langle\mu_T\rangle = \langle\rho\rangle \alpha_1 \frac{3(1+\eta^2)+0.2(\eta^6+\xi^6)}{3+\eta^2+6\eta^2\xi^2+6\xi^2+\eta^6+\xi^6}\frac{K^2}{\epsilon} \tag{20}$$

with

$$\eta^2 = \frac{a_2 K^2}{\epsilon^2} S_{\alpha\beta}S_{\alpha\beta}, \quad \xi^2 = \frac{a_3 K^2}{\epsilon^2} W_{\alpha\beta}W_{\alpha\beta}. \tag{21}$$

The mean rate of strain tensor

$$S_{ij} = \frac{1}{2}\left(\left\langle\!\!\left\langle\frac{\partial u_i}{\partial x_j}\right\rangle\!\!\right\rangle + \left\langle\!\!\left\langle\frac{\partial u_j}{\partial x_i}\right\rangle\!\!\right\rangle\right) \tag{22}$$

and the mean vorticity tensor

$$W_{ij} = \frac{1}{2}\left(\left\langle\!\!\left\langle\frac{\partial u_i}{\partial x_j}\right\rangle\!\!\right\rangle - \left\langle\!\!\left\langle\frac{\partial u_j}{\partial x_i}\right\rangle\!\!\right\rangle\right) \tag{23}$$

while the a-constants $a_1 = (4-3C_2)g/6$, $a_2 = (2-C_3)^2g^2/4$, $a_3 = (2-C_4)^2g^2/4$, $a_4 = (2-C_4)g/2$, $a_5 = (2-C_3)g$, with $g = 2/(C_1+2C_5-2)$. The C constants are determined from the pressure-strain-correlation model:[17] $C_1 = 6.8$, $C_2 = 0.36$, $C_3 = 1.25$, $C_4 = 0.40$, and $C_5 = 1.88$. Finally, the transport coefficients are $\sigma_k = 1.0$, $\sigma_{\epsilon} = 0.16/(C_{\epsilon2} - C_{\epsilon1})C_{\mu L}^{1/2}$ with $C_{\epsilon1} = 1.44$ and $C_{\epsilon2} = 1.83$.

The f function in (17)

$$f = \left[1 - \exp\left(-\frac{y^+}{5.5}\right)\right]^2 \tag{24}$$

is introduced to remove the singularity in the dissipation rate equation at the wall. y^+ is a dimensionless coordinate perpendicular to the wall

$$y^+ = \frac{U_{\tau}\rho y}{\mu}, \tag{25}$$

where $U_{\tau} = (\mu \partial u/\partial y|_{\text{wall}})^{1/2}$ is the friction velocity.

B. K-ϵ turbulence model

The simpler K-ϵ model utilizes a Boussinesq, gradient transport closure for the Reynolds stress tensor[18]

$$\langle\rho\rangle \tau_{ij} \approx \frac{2}{3}\langle\rho\rangle K \delta_{ij} - 2\langle\mu_{TL}\rangle\left(\ll s_{IJ}\gg - \frac{2}{3}\ll S_{\alpha\alpha}\gg \delta_{ij}\right). \tag{26}$$

C. Laminar model

The laminar model is immediately obtained by setting to zero all fluctuations.

III. STEADY STATE 2D MEAN FLOWS OVER TOROIDAL CAVITIES

We consider flow parameters suggested by detached divertor plasma laminar 2D simulations[6] and perform steady state simulations for 2D mean toroidal cavity flow at Reynolds number Re=750, with x in the toroidal direction and y in the radial direction (see Fig. 1). The inflow condition at $x=0$ has a sharp radial temperature profile $T(x=0,y)$, Fig. 2(a), with $T_{\max} = 1.3$ eV and $T_{\text{wall}} = 0.025$ eV. At $x=0$, the inflow radial pressure profile is Gaussian with $p_{\max} = 1$ Torr at toroidal Mach number 1.2. For convenience, we represent

Vahala, Vahala, and Morrison
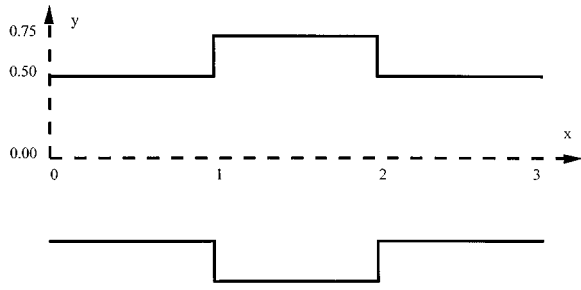
FIG. 1. 2D toroidal cavity geometry, where x is the toroidal and y the radial direction.

(a)

the velocity profiles in Fig. 2 for the full 3D mean flow case—for 2D mean flows one simply sets the poloidal momentum to zero: $\rho w \equiv 0$. The inflow turbulent profiles ρK and $\rho \epsilon$ are taken from simulation data[19] for channel flow and are shown in Fig. 2(b). The symmetry line is $y = 0$, and the toroidal wall is located at $y = 0.5$ [except in the cavity region where the toroidal wall is at $y = 0.75$].

The heat transfer coefficient to the toroidal walls are shown in Figs. 3, with the laminar heat flux always being less than that for the turbulent models. The ASM wall heat flux is greater than that for the K-ϵ model before the cavity, $0 < x < 1$, but the K-ϵ flux is greater within the cavity, $1 < x < 2$, and after the cavity $2 < x < 3$. However, the ratio of these turbulent fluxes is on the order of 1 to 2. The heat flux

(a)

(b)
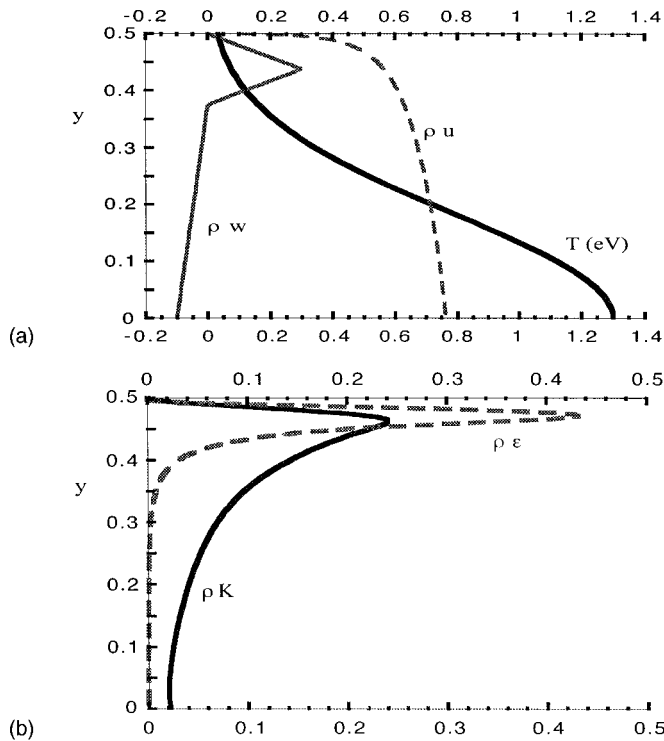
FIG. 2. (a) The inflow radial profiles at $x = 0$ for the temperature T and the toroidal momentum ρu. $y = 0$ is the symmetry line while $y = 0.5$ is the location of the toroidal wall. Of course, for 2D mean flows, there is no poloidal flow $\rho w \equiv 0$. For 3D mean flows, while there is no net poloidal momentum, there is poloidal inflow towards the divertor plate ($0 < y < 0.375$) and poloidal outflow ($0.375 < y < 0.5$). (b) The inflow turbulent radial profiles $\rho \epsilon$ and ρK.
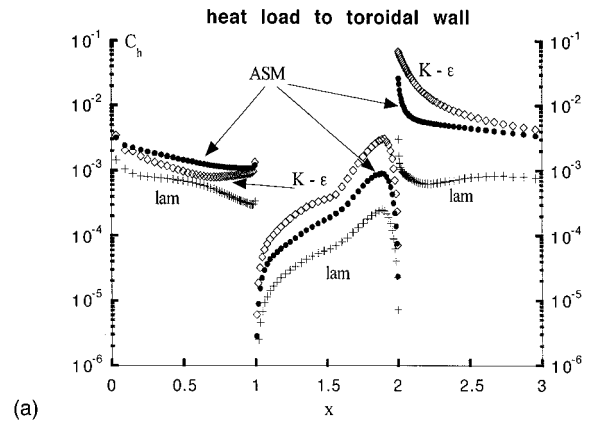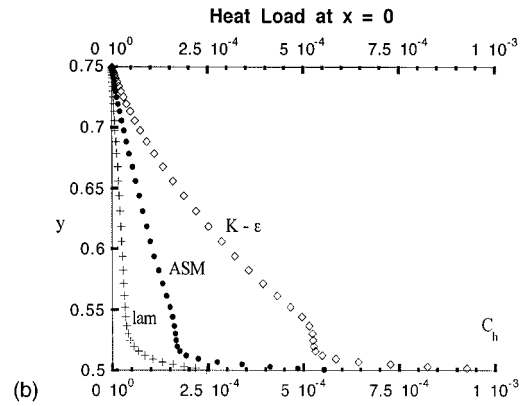
(b)
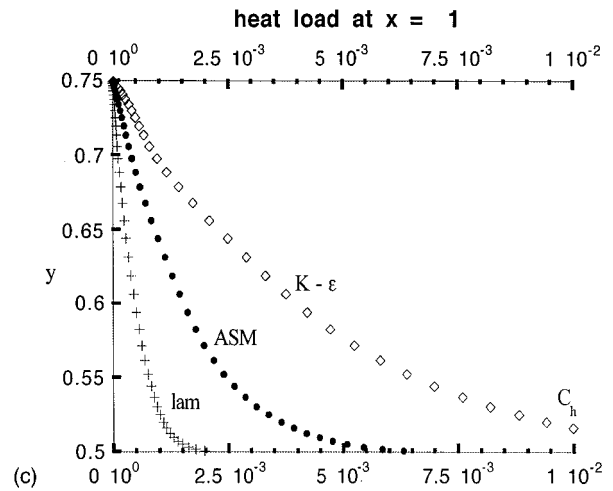
(c)

FIG. 3. Heat flux coefficients to the toroidal walls for ASM, K-ϵ, and laminar flows: (a) toroidal wall $0 < x < 1$, $y = 0.5$; $1 < x < 2$, $y = 0.75$; $2 < x < 3$, $y = 0.5$; (b) leading cavity edge at $x = 1$, $0.5 < y < 0.75$; and (c) trailing cavity edge at $x = 2$, $0.5 < y < 0.75$.

to the trailing edge (at $x = 2$) is typically an order of magnitude greater than that at the leading edge (at $x = 1$), Fig. 3(b) and 3(c). This is to be expected because of flow patterns with the cavity itself.

The corresponding radial temperature profiles are shown in Fig. 4 for three toroidal locations: just before the cavity ($x = 0.9$), within the cavity ($x = 1.5$), and after the cavity ($x = 2.6$). The profiles are shown from the radial symmetry line ($y = 0$) to the toroidal wall ($y = 0.5$ for $x = 0.9$ and $x = 2.6$, and $y = 0.75$ for $x = 1.5$). Before the cavity, $0 < x < 1$, T_{max} is less for the ASM while there is little difference be-
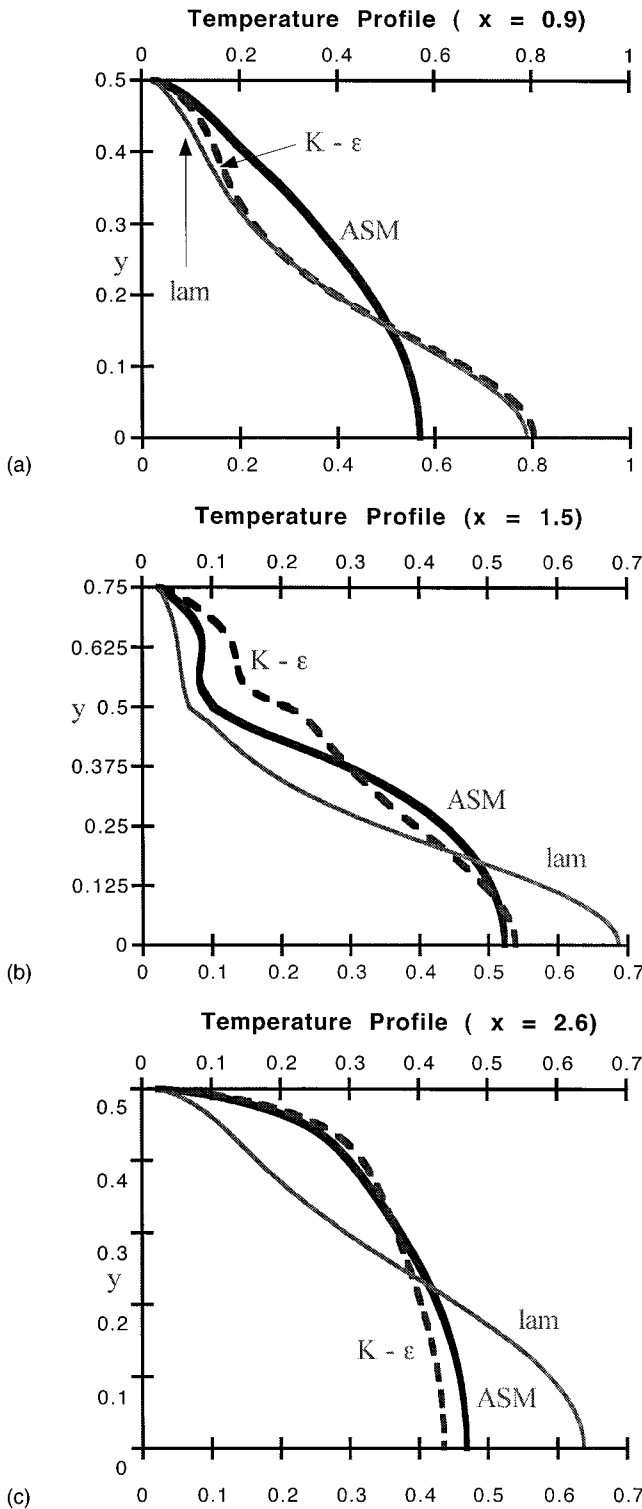
FIG. 4. The radial temperature profiles (a) before the cavity, $x = 0.9$; (b) within the cavity, $x = 1.5$ where now $0 < y < 0.75$; (c) after the cavity, $x = 2.6$.

tween the K-ϵ and laminar profiles. Note that the ASM temperature profile has no inflection point as do the K-ϵ and laminar profiles. Within the cavity and after the cavity, the K-ϵ and ASM profiles are quite similar. One finds in the K-ϵ model, for the flow bordering the cavity region $1 < x < 2$, sharp variations in the turbulent dissipation rate $\rho \epsilon$ around $y = 0.5$ where one finds a very tight steady state shear layer.
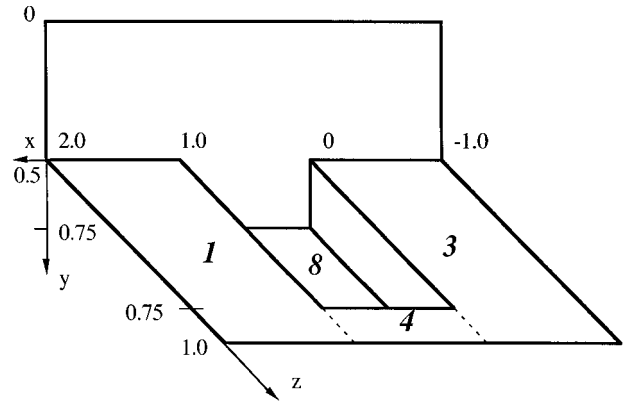
FIG. 5. The 3D toroidal cavity geometry, where x is the toroidal, y the radial, and z the poloidal directions. The divertor plate is at $z = 0$. The input profiles are at $z = 1$.

However, in the ASM this shear layer in the flow bordering the cavity region is quite diffuse because of the effects of the nonlinear strain/vorticity terms.

Because there is little turbulence within the cavity, one finds within the cavity little differences between the ASM, K-ϵ and laminar viscosities. Away from the walls, there is a substantial difference between the ASM and K-ϵ viscosities because of the effects of the mean rate of strain and vorticity, effects that are not present in the definition of the eddy viscosity in the K-ϵ model [compare (18) with (20)]. The effects of shear are more pronounced after the flow passes over the leading edge of the cavity, resulting in an increased ASM eddy viscosity. The eddy viscosity for the K-ϵ model is quite high, even before the cavity, and is considerably reduced in the postcavity region. One should note that the effects of turbulent viscosity on the Reynolds stress τ_{ij}, (19) and (26), are very different between ASM and K-ϵ.

IV. INITIAL VALUE 3D MEAN SHEAR FLOWS OVER TOROIDAL CAVITIES

We now turn to the case of 3D mean shear flow over toroidal cavities. The geometry is shown in Fig. 5. Again, $y = 0$ is the symmetry plane. $z = 0$ is the divertor plate. We label the toroidal wall region as follows:

region 3: $y = 0.5$, $-1 < x < 0$, $0 < z < 1$,

region 4: $y = 0.5$, $0 < x < 1$, $0.75 < z < 1$,

region 1: $y = 0.5$, $1 < x < 2$, $0 < z < 1$,

region 8: $y = 0.75$, $0 < x < 1$, $0 < z < 0.75$.

We consider an initial value problem, with the inflow profiles at $z = 1$ as shown in Fig. 2. Not only is there now a toroidal (ρu) flow of 1.2 Mach number, but also a poloidal flow ρw towards the divertor plate of Mach 0.2 so chosen that there is no net momentum flux to the divertor plate:

$$\int_0^{0.5} dy \rho w = 0. \tag{27}$$

Periodicity is imposed in the toroidal direction ($x = -1$ and $x = 1$).

asm. 19. 3 [peak = 2056]

(a)

turb. 15. 3 [peak = 568]

(b)

lam. 18. 3 [peak = 224]

(c)

asm. 19. 1 [peak = 2045]

(a)

turb. 15. 1 [peak = 569]

(b)

lam. 18. 1 [peak = 224]

(c)
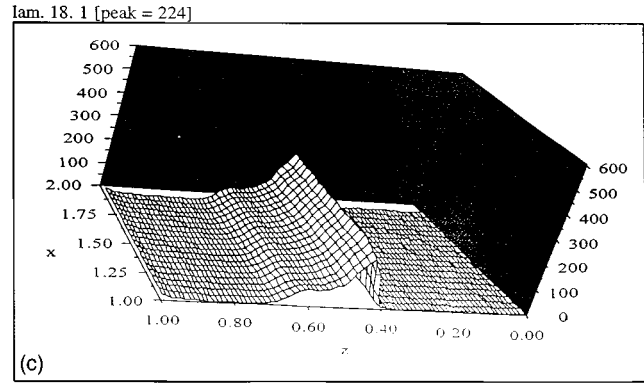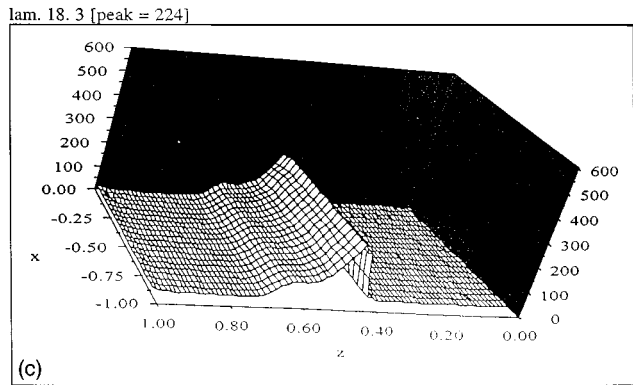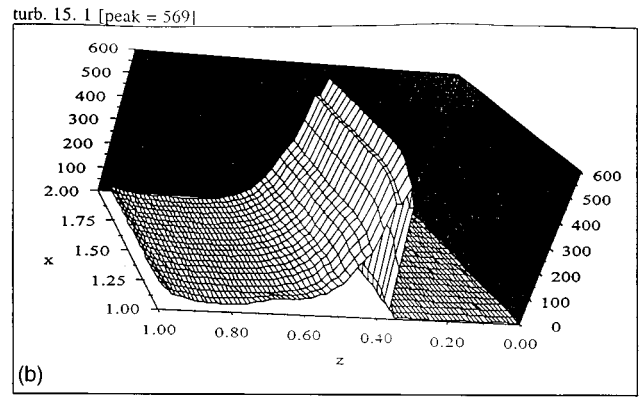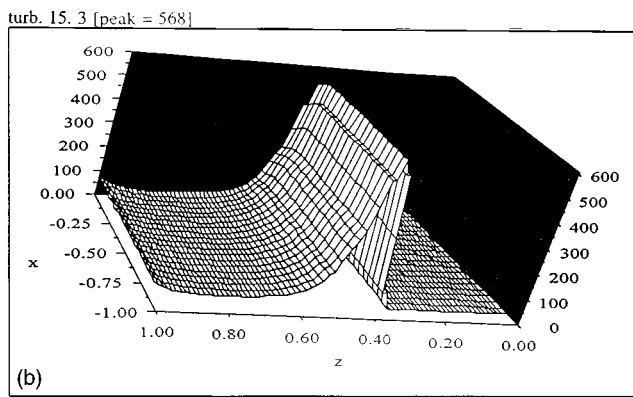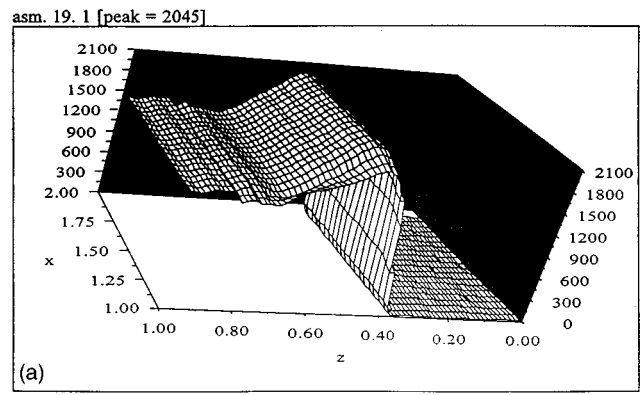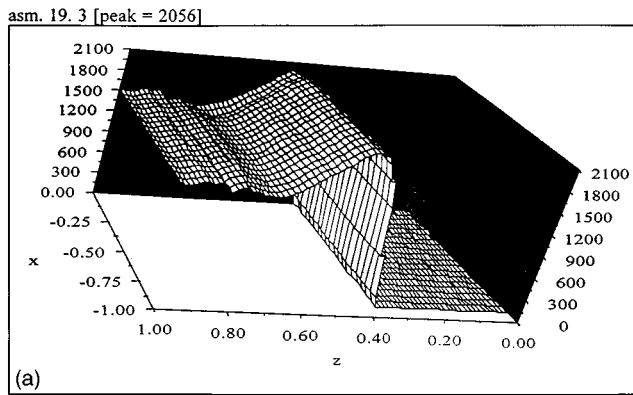
FIG. 6. The heat flux coefficient to that section of the toroidal wall with $-1 < x < 0$ when the heat pulse, which is propagating towards the divertor plate $z = 0$, is at $z = 0.4$. Note the difference in the C_h scales between (a) ASM, (b) K-ϵ, and (c) laminar flows, as well as the considerable ASM heat flux in the wake of the heat pulse.

FIG. 7. The heat flux coefficient to that section of the toroidal wall with $1 < x < 2$ when the heat pulse, which is propagating towards the divertor plate $z = 0$, is at $z = 0.4$. Note the difference in the C_h scales between (a) ASM, (b) K-ϵ, and (c) laminar flows, as well as the considerable ASM heat flux in the wake of the heat pulse.

In what follows, we shall examine the heat flux coefficient $C_h(x,z)$ to the toroidal wall as the heat pulse propagates towards the divertor plate, $z = 0$. We find very significant differences between all 3 models: the turbulent ASM, K-ϵ, and laminar flows. When the heat pulse is located at $z \approx 0.4$, the corresponding heat flux coefficient $C_h(x,z)$ to the toroidal wall is plotted in Figs. 6–8 for regions 3, 1, and 4. One notes there is little difference in the toroidal wall heat flux to regions 3 (Fig. 6) and 1 (Fig. 7). As expected, the maximum in C_h occurs at $z = 0.4$ but the peak in the turbulent ASM model is nearly a factor of four greater than in the turbulent K-ϵ model while nearly a factor of ten greater than for laminar flow. In the K-ϵ and laminar cases, the toroidal wall heat flux coefficients are quite localized, with $C_h \approx 0$ in

the tail of the heat front $0.6 < z < 1.0$. However, in the ASM model, the wall heat flux in the tail region of the heat pulse remains high—a factor of three greater than the peak of the wall flux for the K-ϵ model. This effect is very evident in region 4, Fig. 8, which is in the tail of the heat pulse. These major differences between the ASM and K-ϵ turbulence models arise because of the nonlinear effect of the quadratic mean vorticity and/or velocity strain tensors [cf (19) and (20)]—effects which are enhanced by the cavity region. The cavity region also has a profound effect on the C_h in region 8. When the heat pulse is at $z \approx 0.4$, there is negligible toroidal heat flux to the cavity floor.

Similar full toroidal wall heat flux C_h (for ASM, K-ϵ, and laminar flows) results are shown in Fig. 9 when the pulse

Phys. Plasmas, Vol. 4, No. 11, November 1997

Vahala, Vahala, and Morrison   3997
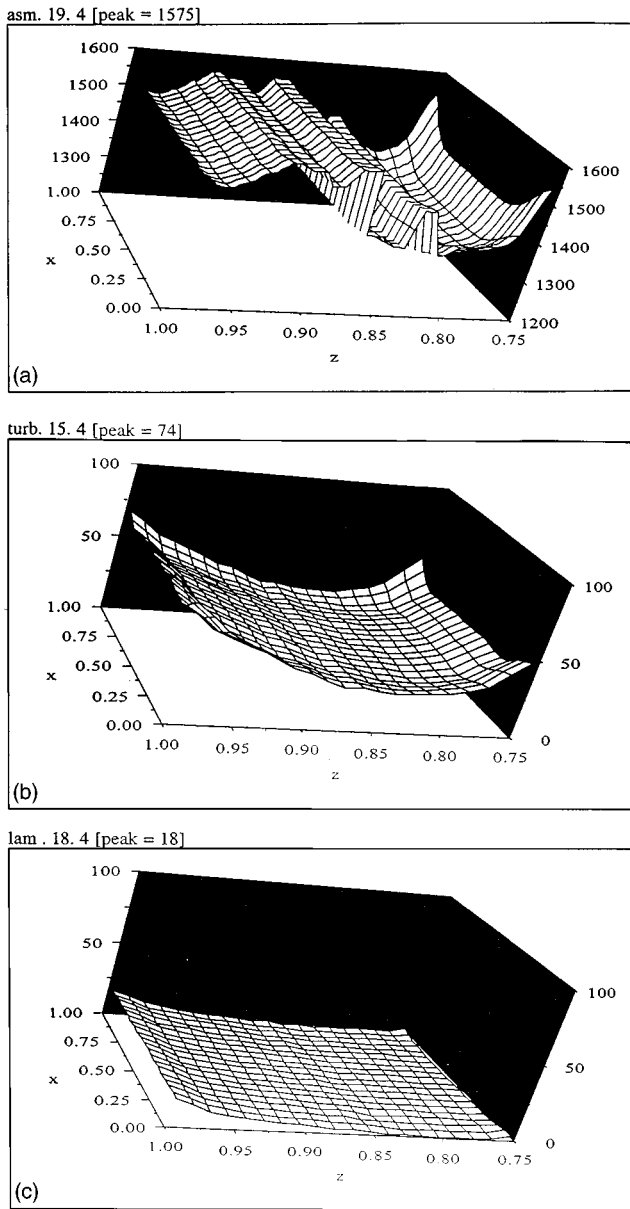
FIG. 8. The heat flux coefficient to the $0<x<1$, $0.75<z<1$ section of the toroidal wall in the wake of the heat pulse located at $z=0.4$. Note the difference in the C_h scales between (a) ASM, (b) K-ϵ, and (c) laminar flows. The ASM C_h is over a factor of 20 greater than the K-ϵ C_h.

FIG. 9. The full toroidal heat flux coefficients when the heat pulse is at $z=0.15$. (a) ASM, (b) K-ϵ, and (c) laminar.

is at $z\approx0.15$. There is now some heat flux to the cavity floor, but this flux (in all three models) is delayed till $z\approx0.4$. Again, one sees the long wall heat flux in turbulent ASM model in the tail behind the pulse.

V. NUMERICAL CODE ISAAC

We now briefly comment on the code[20] ISAAC (Integrated Solution Algorithm for Arbitrary Configurations). The equations to be solved are written in the form of inviscid (convective) fluxes, viscous (diffusive) fluxes, and source terms. In the finite-volume discretization, the particular scheme used depends on how one approximates the interface flux of the computational cell bounding the cell-averaged quantities. ISAAC was written with the goal of good shock capturing, good accuracy, and general geometric capabilities. A Roe approximate Riemann solver is coupled with a (MUSCL) scheme to achieve second-order spatial accuracy for the inviscid terms. Consistent with the elliptic nature of the diffusive fluxes, a finite-volume representation of a

Vahala, Vahala, and Morrison

second-order accurate central-difference operator is employed. The source terms are treated as an integral over the control volume. To accommodate geometrically complex configurations, a multiblock procedure is implemented that requires C^0 grid continuity. In ISAAC, one employs a first-order implicit scheme for steady-state simulations and a second-order implicit scheme for time-dependent simulations. The algorithm has been validated on both 2D and 3D mean flows. In our steady state runs, convergence was deemed to have been reached when the residuals had dropped by at least four orders of magnitude, while for the time-dependent runs the residuals are checked during the time subiterations.

The code has been benchmarked against experimental data on subsonic and supersonic boundary layers, supersonic mixing layers, supersonic flow past ramps up to deflection angles of 24°, and transonic airfoils by comparing the pressure, mean velocities, skin friction as well as turbulent statistics.[13,20,21] In the 2D simulations, the regular channel $0 < x < 3$, $0 < y < 0.5$ grid was 121×101 while in the cavity region ($1 < x < 2$, $0.5 < y < 0.75$), the grid was 41×41. One iteration takes approximately 1 s on the J90, with approximately 70 K iterations to reach steady state. For the 3D simulations, in the regular 3D volume ($-1 < x2$, $0 < y < 0.5$, $0 < z < 1$) the numerical grid was $61 \times 101 \times 81$, with a $21 \times 21 \times 61$ grid in the cavity volume ($0 < x < 1$, $0.5 < y < 0.75$). Typical storage requirements were 120 MW, and one iteration takes approximately 18 min.

Finally, we comment on the numerical accuracy of our results. In Fig. 10, for regions 3 and 1, the surface plot of the dimensionless coordinate y^+, (25), is shown for the ASM model when the heat pulse is at $z \approx 0.4$. For nearly all the surface, $y^+ < 0.2$—except in the region $x \approx 0$ and $x \approx 1$ near the pulse leading edge ($z \approx 0.4$). This is somewhat expected since the start of the cavity domain is at $x = 0$ and the end of the cavity domain is $x = 1$. Past calculations have shown that this resolution is sufficient to resolve both velocity and temperature gradients in the near-wall region so that the wall heat-transfer rates computed are reliable. However, our 3D resolution is inadequate to resolve the heat flux to the divertor plate when the heat pulse hits the target plate.

VI. CONCLUSION

Here we have considered wall heat flux in shear flows over toroidal cavities using ASM and K-ϵ turbulence models and compared them to the corresponding laminar results. First, we determined the steady state toroidal heat flux wall due to a sharp temperature gradient propagating in 2D mean flows. It is found that the simple K-ϵ model typically overestimates the heat fluxes while the inclusion of mean vorticity effects (absent in the simple K-ϵ model) leads to slightly reduced fluxes. The steady state radial turbulent temperature profiles are quite similar, especially within the cavity and postcavity regions. Turbulence significantly increases the heat loads to the toroidal wall and this lessens the impact on the divertor plate.

When one considers 3D mean shear flows by including the poloidal flow towards the divertor plate itself, it is easier to pose an initial value problem: what is the toroidal wall
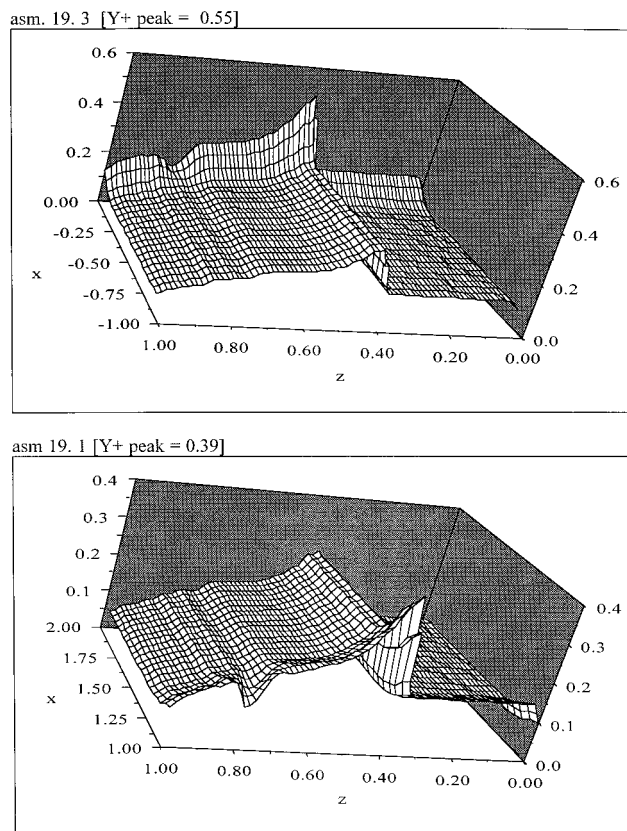
FIG. 10. Plots of y^+ for ASM when the heat pulse is located at $z = 0.4$ for regions 3 and 1 in Fig. 5.

heat load as a heat pulse propagates along field lines towards the divertor plate? We find very significant increases to the toroidal heat flux due to the quadratically nonlinear terms in mean shear and mean vorticity of the ASM over the simpler K-ϵ turbulence model—especially in the wake of the heat pulse—due to the toroidal cavities.

We do not present any results for the heat flux to the divertor plate as the heat pulse hits the target plate since our resolution is inadequate. Efforts are underway to parallelize the simulation code ISAAC so that finer 3D grids can be employed. The formulation of the steady-state toroidal heat load problem for 3D mean shear flows is under consideration.

ACKNOWLEDGMENTS

[1]G. Janeschitz, J. Nucl. Mater. **220–222**, 67 (1995).
[2]B. Lehnert, Nucl. Fusion **8**, 173 (1967).
[3]A. V. Nedospasov and M. Z. Tokar', in *Reviews Plasma Physics* edited by B. B. Kadomtsev (Consultants Bureau, New York, 1993), Vol. 18, p. 77.
[4]S. I. Krasheninnikov and A. Yu. Pigarov, in *Plasma Physics and Con-*

trolled Nuclear Fusion Research 1986 (International Atomic Energy Agency, Vienna, 1987), Vol. 1, p. 387; A. Yu. Pigarov and S. I. Krasheninnikov, Phys. Lett. A **222**, 251 (1987).

[5]G. Janeschitz, S. Clement, N. Gottardi, M. Lesourd, J. Lingertat, C. Lowry, G. Radford, G. Saibene, M. Stamp, D. Summers, A. Taroni, P. R. Thomas, and G. Vlases, in *Proceedings of 19th European Conference on Controlled Fusion and Plasma Physics*, Innsbruck, 1992 (European Physical Society, Petit-Lancy, Switzerland, 1992), Vol. 16C, Part II, p. 727; T. W. Petrie, D. Buchenauer, D. N. Hill, C. Klepper, S. Allen, R. Campbell, A. Futch, R. J. Groebner, A. Lenoard, S. Lippmann, M. Ali Mahdavi, M. Rensink, and P. West, J. Nucl. Mater. **196–198**, 848 (1992); V. Mertens, K. buchl, W. Junker, F. Mast, M. Schittenhelm, M. Bessenrodt-Weberpals, A. Field, Ch. Fuchs, O. Gehre, O. Gruber, A. Herrmann, G. Haas, A. Kallenbach, H. Kastelewicz, M. Kaufmann, W. Koppendorfer, M. Laux, G. Lieder, J. Neuhauser, F. Ryter, H. Salzmann, W. Sandmann, K.-H. Steurer, A. Stabler, H. Zohm, and the Asdex Upgrade Team, in *Proceedings of the 20th European Conference on Controlled Fusion and Plasma Physics*, Lisboa, 1993 (European Physical Society, Petit-Lancy, Switzerland, 1993), Vol. 17C, Part I, p. 267; I. H. Hutchinson, R. Boivin, F. Bombarda, P. Bonoli, S. Fairfax, C. Fiore, J. Goetz, S. Golovato, R. Granetz, M. Greenwald, S. Horne, A. Hubbard, J. Irby, B. LaBombard, B. Lipschultz, E. Marmar, G. McCracken, M. Porkolab, J. Rice, J. Snipes, Y. Takase, J. Terry, S. Wolfe, C. Christensen, D. Garnier, M. Graf, T. Hsu, T. Luke, M. May, A. Nemczewski, G. Tinios, J. Schachter, and J. Urban, Phys. Plasmas **1**, 1511 (1994).

[6]D. A. Knoll, P. R. McHugh, S. I. Krasheninnikov, and D. J. Sigmar, Phys. Plasmas **3**, 293 (1996); F. Wising, D. A. Knoll, S. I. Krasheninnikov, T. D. Rognlien, and D. J. Sigmar, Contr. Plasma Phys. **36**, 309 (1996)

[7]G. D. Porter, S. L. Allen, M. Brown, M. E. Fenstermacher, D. N. Hill, R. A. Jong, A. W. Lenoard, D. Nilson, M. E. Rensink, T. D. Rognlien, G. R. Smith, and DIII-D team, Phys. Plasmas **3**, 1967 (1996); D. E. Post, J. Nucl. Mater. **220–222**, 143 (1995).

[8]S. I. Krasheninnikov, A. Yu. Pigarov, D. A. Knoll, B. LaBombard, B. Lipschultz, D. J. Sigmar, T. K. Soboleva, J. L. Terry, and F. Wising, Phys. Plasmas **4**, 1638 (1997).

[9]J. S. Kapat, J. Ratnathicam, and B. B. Mikic, J. Fluids Eng. **116**, 484 (1994).

[10]G. Vahala, L. Vahala, J. Morrison, S. Krasheninnikov, and D. Sigmar, Phys. Lett. A **205**, 266 (1995); Contr. Plasma Phys. **36**, 329 (1996); J. Plasma Phys. **57**, 155 (1997).

[11]R. S. Rogallo and P. Moin, Annu. Rev. Fluid Mech. **16**, 99 (1984).

[12]T. B. Gatski, ''Turbulent flows: model equations and solution methodology,'' in *Handbook of Computational Fluid Mechanics*, edited by R. Peyret, (Academic, London, 1996).

[13]A. Favre, J. Mec. **4**, 361 (1965).

[14]T. B. Gatski and C. G. Speziale, J. Fluid Mech. **254**, 59 (1993).

[15]R. Abid, J. H. Morrison, T. B. Gatski, and C. G. Speziale, AIAA J. **34**, 2632 (1996).

[16]S. B. Pope, J. Fluid Mech. **72**, 331 (1975).

[17]C. G. Speziale, S. Sarkar, and T. B. Gatski, J. Fluid Mech. **227**, 245 (1991).

[18]H. S. Zhang, R. M. C. So, T. B. Gatski, and C. G. Speziale, in *Near-Wall Turbulent Flows*, edited by R. M. C. So, C. G. Speziale, and B. E. Launder (Elsevier Science, Amsterdam, 1993), pp. 209.

[19]P. Spalart, J. Fluid Mech. **187**, 61 (1988).

[20]J. H. Morrison, ''A Compressible Navier-Stokes Solver with Two-Equation and Reynolds Stress Turbulence Closure Models,'' National Aeronautical and Space Administration Contractor Report 4440 (National Aeuronautics and Space Administration, Washington, D.C., May 1992).

[21]J. H. Morrison, T. B. Gatski, T. B. Sommer, H. S. Zhang, and R. M. C. So, in *Near-Wall Turbulent Flows*, edited by R. M. C. So, C. G. Speziale, and B. E. Launder (Elsevier Science, Amsterdam, 1993), p. 239.